ELSEVIER

Contents lists available at ScienceDirect

Acta Materialia

journal homepage: www.elsevier.com/locate/actamat



Effect of rapid solidification and post-processing on microstructure, magnetic and structural transition temperatures and magnetic properties in Ni₅₀Mn₂₉Ga₂₁ magnetic shape-memory alloy

Emily Flitcraft^a, Pierangeli Rodriguez De Vecchis^b, Alexey Kuprienko^a, Markus Chmielus^b, Carolin Fink^{a,*}

ARTICLE INFO

Keywords: Ferromagnetic shape memory alloys Rapid solidification Magnetic properties Ni-Mn-Ga

ABSTRACT

This study investigated the effect of rapid solidification and post-processing on microstructure, composition and magneto-structural properties of $Ni_{50}Mn_{29}Ga_{21}$ (at.%) magnetic shape memory alloy (MSMA). Samples with varying cooling rates $(1.1 \bullet 10^2 \text{ to } 3.2 \bullet 10^3 \text{K/s})$ were prepared using arc melting for a comparative study in assolidified condition and after two different heat treatments. A notable change from columnar-dendritic to cellular-dendritic solidification and a decrease in solidification length scale was observed at more rapid solidification. All samples showed Mn enrichment and corresponding Ga depletion at the sub-grain boundaries. The fine-scale solidification structure, chemical heterogeneity and lack of ordering resulted in broad martensitic transformations. At more rapid solidification, a decrease in saturation magnetization and abnormal slope changes in the hysteresis loop were observed. Heat-treatment resulted in grain growth, significant reduction in transformation breadth, and increase in magnetization saturation. Rapidly solidified samples with an estimated characteristic cooling rate of $1.1 \bullet 10^3 \text{K/s}$ most closely resembled microstructures and magneto-structural properties from laser directed energy deposition (L-DED) processing. The results of this study help to understand cooling rate effects in L-DED additive manufactured Ni-Mn-Ga and provide post-processing routes that will result in microstructures and properties that resemble those of functional MSMA.

1. Introduction

Ferromagnetic Ni-Mn-Ga shape memory alloys are attractive candidates for applications as actuators [1,2], and sensors [3] due to their ability to develop large and fast reversible pseudo-plastic strains when exposed to a magnetic field. Magnetic field induced strains (MFIS) are produced when twin variants of the ferromagnetic martensitic phase rearrange in response to magnetically induced stress. Single crystalline Ni-Mn-Ga exhibits the largest MFIS of up to 6–12% [4–6]. In bulk polycrystalline alloys grain boundary constraints generally prevent MFIS, although moderate MFIS has been demonstrated in specifically structured polycrystalline foams (up to 8.7%) [7] and strongly textured polycrystalline Ni-Mn-Ga (up to 4%) [8]. As a result, processing methods for the manufacturing of functional Ni-Mn-Ga based devices are limited. In addition, Ni-Mn-Ga alloys are difficult to machine due to their brittleness, which imposes additional geometric constraints.

To address these challenges, an increasing interest in utilizing additive manufacturing (AM) methods has been seen in recent years. Binder jet processes, such as 3D ink printing [9,10], and sintered binder jet printing [11–14] have proven feasible for producing polycrystalline foam-like Ni-Mn-Ga structures with complex geometries. More recently, research utilizing laser additive manufacturing, namely laser-based direct energy deposition (L-DED) [15] and laser powder bed fusion (L-PBF) [16-18], has demonstrated deposition of bulk polycrystalline Ni-Mn-Ga. However, the non-equilibrium conditions associated with this layer-by-layer fusion-based process (including melting, resolidification and complex thermal cycling with rapid heating and cooling) creates challenging microstructures characteristic of nonfunctional or low-functional alloys [15,16,19-21],. It has been shown that post-process heat treatment for chemical homogenization and atomic ordering can significantly improve the magneto-structural properties of the builds [22]. However, the production of foam-like lattice structures

E-mail address: fink.242@osu.edu (C. Fink).

^a Department of Materials Science and Engineering, The Ohio State University, Columbus, OH 43221, United States

b Department of Mechanical Engineering and Materials Science, University of Pittsburgh, Pittsburgh, PA 15261, United States

 $^{^{\}ast}$ Corresponding author.

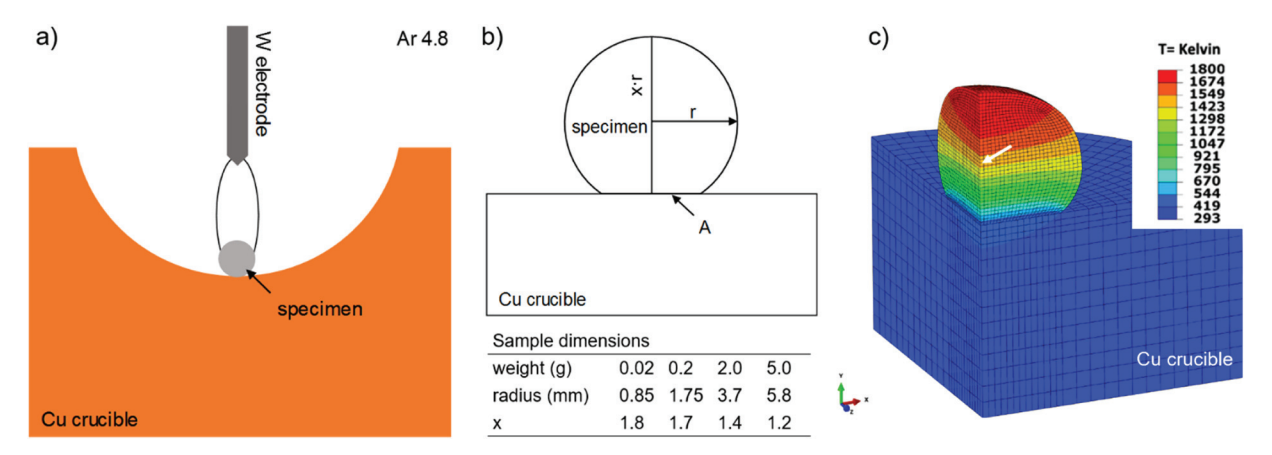


Fig. 1. (a) Schematic of physical simulation for rapid solidification via tungsten electrode arc melting, (b) sample dimensions used for thermal analysis via finite element method, and (c) meshed sample, showcasing quarter symmetry model, isotherm distribution and center location for cooling curve extraction (arrow).

with enhanced crystallographic texture will need to be targeted in the future in order to obtain sufficient MFIS from laser additive Ni-Mn-Ga [18,22,23],. To achieve this goal, it is crucial to understand the effect of processing conditions on microstructural and compositional homogeneity, and resulting phase constitution and magnetic properties of the as-deposited material. Previous work focused on the effect of laser process parameters, primarily laser power and scanning speed [16,17]. Research that directly varied fast or rapid solidification in Ni-Mn-Ga to investigate its effect on material properties is limited. Chernenko et al. [24] reported that higher spinning speed (i.e., faster solidification) in melt-spun Ni-Mn-Ga ribbons resulted in a decrease of the structural transformation temperatures and the Curie temperature. This was attributed to an increase in short range chemical disorder and/or internal stresses from rapid quenching. Wang et al. [25] observed no change of the martensite transformation temperatures in rapidly quenched Ni-Mn-Ga ribbons, but a significantly decrease in Curie temperature and saturation magnetization. The authors reported that quenched-in residual stresses from more rapid solidification resulted in an increased magnetic field needed for twin boundary motion [25]. Cooling rates in melt spinning (10^5-10^7K/s) [26,27], are similar to what is experienced during L-PBF processes [28], but are typically higher than cooling rates expected in L-DED (10²-10⁴K/s) [29,30],. The present study aims to fill this gap by systematically investigating the effect of rapid solidification on the microstructure, magnetic and structural transformation temperatures and resultant magnetic properties of Ni₅₀Mn₂₉Ga₂₁ alloy. Rapid solidification experiments with varying cooling rates were conducted on small samples. Heat transfer analysis using finite element method was employed to estimate the cooling rate of the samples (between $1.1 \cdot 10^2$ and $3.2 \cdot 10^3$ K/s). A detailed comparative study was conducted on the microstructural, compositional and magneto-structural properties of the rapidly solidified Ni₅₀Mn₂₉Ga₂₁ samples in both the as-solidified condition and after two different heat treatments. The findings were then compared to microstructures and properties of samples built via laser-based direct energy deposition (L-DED).

2. Materials and methods

An ingot (approx. 45g) with nominal composition $Ni_{50}Mn_{29}Ga_{21}$ was prepared via induction melting of pure alloying elements (at least 99.95% purity). The composition was chosen to be similar to what was used by Toman et al. [15] to prepare an actual Ni-Mn-Ga build using laser-based direct energy deposition (L-DED). The prepared ingot was crushed into smaller pieces. Rapid solidification experiments were performed by re-melting and rapidly cooling of small samples (0.02, 0.2, 2.0 and 5.0g) using tungsten electrode arc melting in a water-cooled copper crucible in argon atmosphere. The electric arc was ignited directly above

the sample and extinguished as soon as the sample was fully melted. Arc current was 75 A and arc time ranged from about 1 to 10s depending on sample size. Fig. 1a shows a schematic of the setup for the rapid solidification experiments. This approach was originally developed by Kenel and Leinenbach [31] for characterization of microstructure formation in rapidly solidified alloys and successfully applied to binary Ti-Al alloys.

Finite element method was employed to estimate cooling rates as a function of sample size. Heat transfer analysis was carried out in Abaqus/CEA 2021 software using full integration 8-node linear heat transfer elements (DC3D8). The element size for a specimen was 1/50th of its diameter. The shapes and dimensions of actual re-melted samples were digitized using Engauge Digitizer software and imported to Abaqus (Fig. 1b). The copper crucible was simplified to a shape of a straight cylinder with a finer mesh at the interface to the sample. For computational efficiency, a quarter symmetry model was utilized for thermal analysis, as shown in Fig. 1c. The initial temperature of the crucible was set to 293K. Convective heat transfer was considered between the crucible and its surroundings to simulate both water cooling at the base and air cooling at the side surface. Convective heat transfer was also

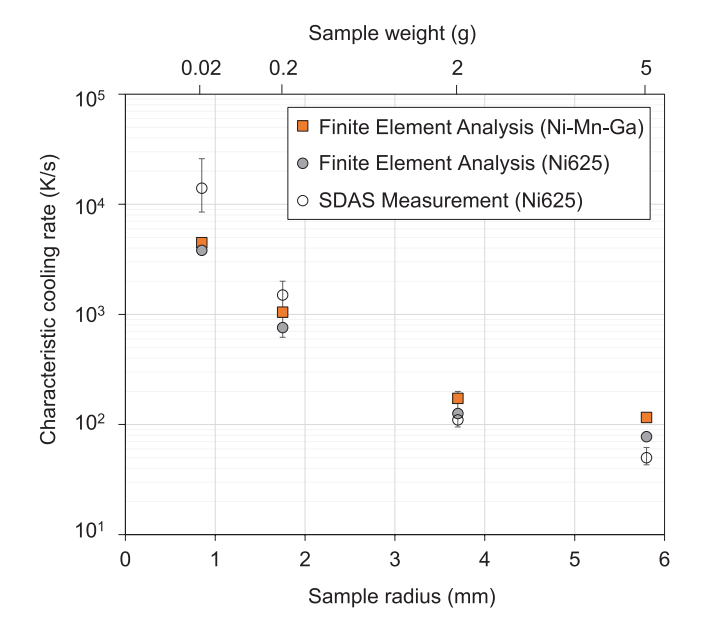


Fig. 2. Characteristic cooling rates from finite element analysis for Ni-Mn-Ga alloy (orange squares) as a function of sample radius (sample weight). Simulated cooling rates are compared to cooling rates from secondary dendrite arm spacing (SDAS) measurements for nickel-based alloy 625 (Ni625) for verification purposes (filled and open circles, respectively).

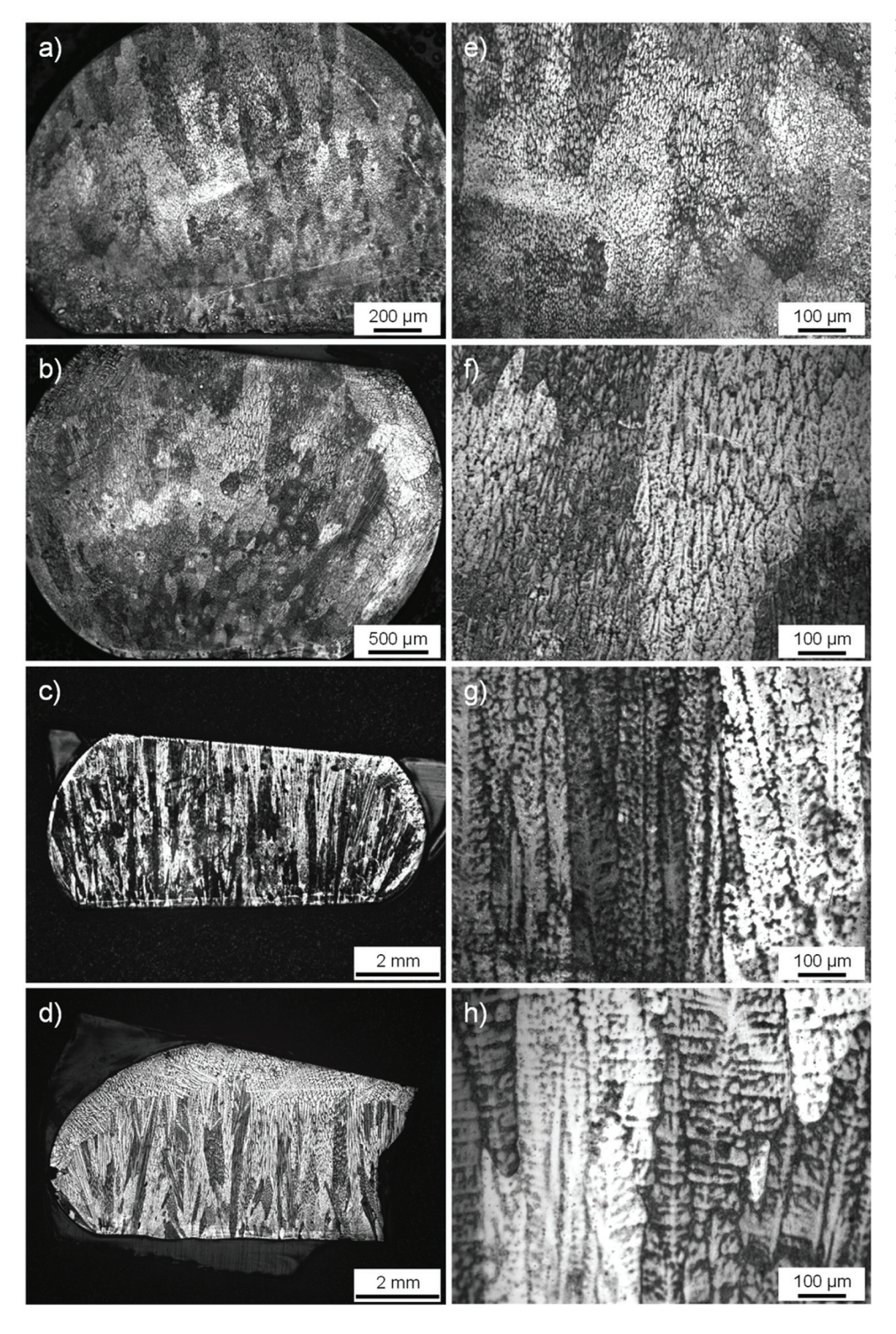


Fig. 3. Optical micrographs (etched) of the assolidified microstructure for the 0.02g (a, e), 0.2g (b, f), 2g (c, g) and 5g (d, h) Ni-Mn-Ga samples. Note the difference in magnification for the lower magnification images (a-d). The close-up of the solidification structure is shown at the same magnification for all samples for comparison purposes. Note the increase in solidification length scale with increasing sample size (decreasing characteristic cooling rate), and the accompanying change from cellular-dendritic to columnar-dendritic solidification.

accounted for at the surface of the sample. Conductive heat transfer was modeled at the contact interface between the copper crucible and the sample. Thermo-physical properties for Ni-Mn-Ga were taken from published data for a Ni₂MnGa alloy [32]. The thermal conductivity used for copper was 398 and 357W/(m•K) at 298 and 1000K, respectively [33].

For transient heat transfer analysis, the initial temperature of the liquid alloy sample was set to 1800K. This temperature was chosen based on maximum temperatures measured using infrared thermal imaging during electrode arc melting of $Ni_{50}Mn_{29}G_{21}$. As shown in Fig. 1c, nodal temperatures in the center of the sample were extracted from the

finite element model as a function of cooling time and used for cooling rate analysis. The characteristic cooling rate was defined as the cooling rate before solidification, i.e., the mean slope of the cooling curve between 1800 and 1423K. This temperature range was chosen based on the liquidus temperature for Ni₂MnGa of $T_L=1405 \mathrm{K}$ [32].

Fig. 2 shows the obtained cooling rates from the finite element analysis as a function of sample radii. The cooling rates varied from $1.1 \cdot 10^2$ to $3.2 \cdot 10^3$ K/s with varying sample weight (radii) from 0.02g (0.85mm) to 5.0g (5.8mm). For verification of the finite element simulations, cooling rates were estimated based on the scale of the solidification structure of electrode arc melted samples. This relation is based

Table 1 Solidification morphology, bulk composition with standard deviations of the assolidified samples and calculated partition coefficients from SEM-EDS line scan data.

Sample weight	Solidification morphology	Compo	sition (at.	-%)	Partition coefficient (k_{eff})			
		Ni	Mn	Ga	k-Ni	k- Mn	k- Ga	
0.02 g	Cellular- dendritic	51.2 ±0.2	27.8 ±0.2	21.0 ±0.3	1.00	0.98	1.01	
0.2 g	Cellular- dendritic	49.4 ±0.3	$\begin{array}{c} 29.8 \\ \pm 0.8 \end{array}$	20.8 ± 0.6	1.00	0.98	1.02	
2 g	Columnar- dendritic	49.5 ±0.3	$29.8 \\ \pm 0.7$	20.7 ± 0.5	1.01	0.94	1.05	
5 g	Columnar- dendritic	$\begin{array}{c} 49.8 \\ \pm 0.4 \end{array}$	$\begin{array}{c} 28.7 \\ \pm 1.0 \end{array}$	$\begin{array}{c} 21.5 \\ \pm 0.6 \end{array}$	1.00	0.96	1.04	

on the solidification time being inversely proportional to the cooling rate [34]. Quantitative correlations between cooling rate and cell or dendrite arm spacing are not available in the literature for Ni-Mn-Ga but are well established for some nickel-based alloys [35,36]. The latter also being close in density to Ni₂MnGa ($\rho=8.16\rm g/cm^3$), which results in similar sample dimensions. Samples for rapid solidification via tungsten electrode arc melting were prepared from commercial nickel-based alloy 625 ($\rho=8.44\rm g/cm^3$). Secondary dendrite arm spacing (SDAS) was measured on etched cross-sections using ImageJ software [37]. The following relation correlates secondary dendrite arm spacing λ in microns to the cooling rate before solidification ε (K/s):

$$\lambda = A \cdot \varepsilon^{-n}$$

where A and n are material constants, which Tinoco and Fredriksson [35] determined to be 58.02 and 0.312 for alloy 625, respectively. As shown in Fig. 2, calculated cooling rates from dendrite arm spacing measurements are in good agreement with simulated cooling rates from finite element analysis for nickel-based alloy 625. Discrepancies are highest at the smallest sample size, where cooling rates from dendrite arm spacing are higher than in the simulation. Based on the reasonable agreement between experimental and simulated cooling rates for alloy 625, the characteristic cooling rates from finite element analysis are assumed to be representative for the studied Ni-Mn-Ga samples. The cooling rate for the smallest sample size (0.02g) may be somewhat higher than what is obtained from finite element analysis. For convenience, the rapidly solidified Ni-Mn-Ga samples are hereafter named 0.02, 0.2, 2 and 5g corresponding to their weight, with the smallest sample experiencing a characteristic cooling rate two orders of magnitude higher than the largest sample (Fig. 2).

Ni₅₀Mn₂₉Ga₂₁ samples from rapid solidification experiments were cross-sectioned through the center for microstructural analysis, embedded in epoxy resin, and polished and etched with a mixture of 4mg Cu₂SO₄, 20ml HCl and 20ml H₂O (Marble's reagent) for imaging under an Olympus GX-51 light optical microscope. Scanning electron microscopy (SEM) and energy dispersive spectroscopy (EDS) were performed on polished and unetched samples in an FEI Apreo SEM to image

the solidification microstructure at higher magnification and obtain compositional information from the bulk and on potential segregation of elements during solidification. Images acquired from backscattered electron signal in the SEM were used for analysis of the scale of the solidification structure in ImageJ software [37]. X-ray diffraction (XRD) was performed in a Bruker X8 Prospector Ultra, using 45kV voltage, 0.65mA current, and 150mm detector distance, complete 0–360° phi rotation per location, 30–100° 2theta range and 216s/image.

For structural and magnetic transition temperature analysis, samples from rapid solidification were manually crushed into smaller pieces (ranging from 0.02 to 0.04g). Differential scanning calorimetry (DSC) was conducted from 0 to 140°C with a TA instrument DSC2500 at a rate of 5°C/min . A Quantum Design MPMS 3 SQUID system was used in Vibrating Sample Magnetometer (VSM) mode to measure magnetization as a function of temperature from 26 to 120°C at a constant field of 10 mT. Measurements were also performed as a function of applied magnetic field ranging up to 2 T (hysteresis loop).

Finally, samples from rapid solidification experiments (0.2 and 2g only) were encapsulated in an argon atmosphere and subjected to two different heat treatment procedures. One set of samples was subjected to a short-term chemical homogenization heat treatment at 1000° C for 1h and subsequently water quenched. Another set of samples was

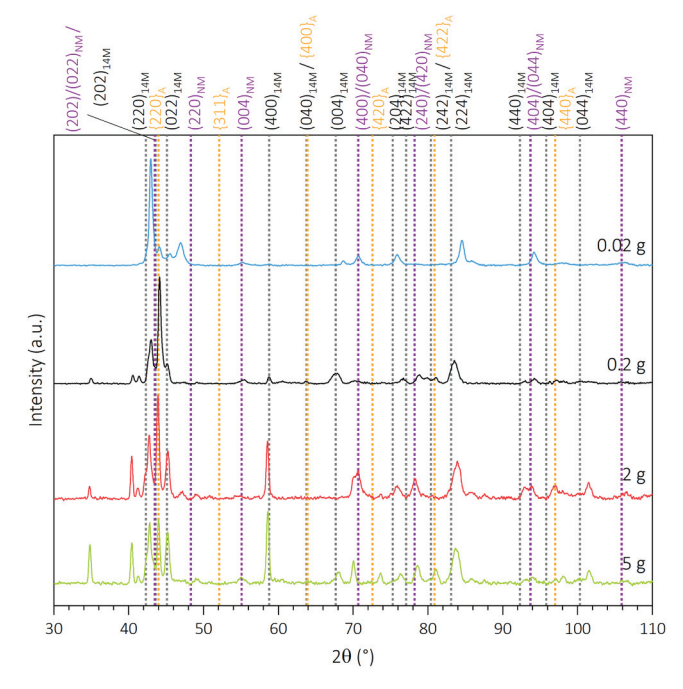


Fig. 5. XRD patterns obtained for the as-solidified Ni-Mn-Ga samples. Gray dashed lines indicate the 14M martensite peak locations, purple dashed lines indicate the NM martensite peak locations (calculated using the 0.2g sample), and orange dashed lines the austenite (A) locations, as shown at the top of the graph

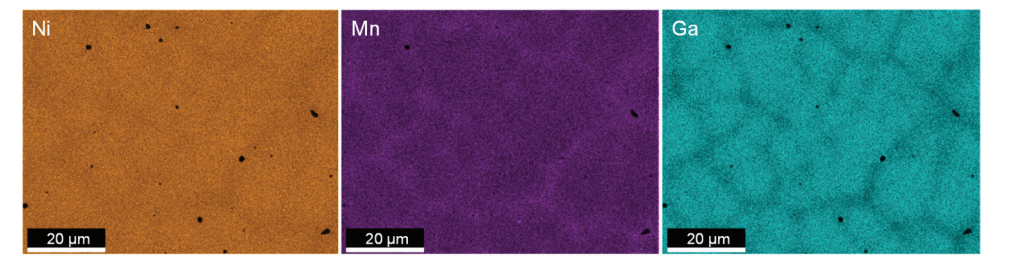


Fig. 4. Compositional map (SEM-EDS) across the as-solidified microstructure of the 0.02g sample. Note the enrichment of Mn and corresponding depletion of Ga at the cell boundaries.

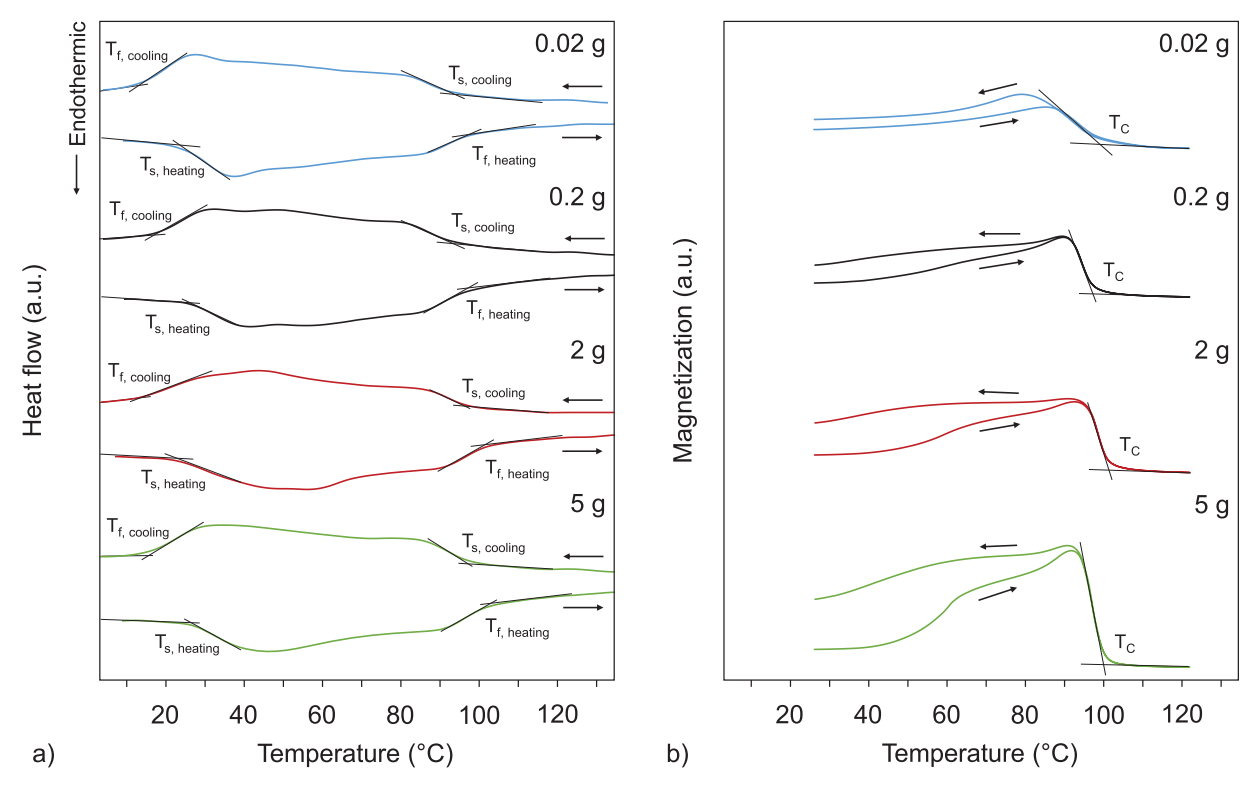


Fig. 6. Heat flow versus temperature curves from DSC (a) and curves from magnetization versus temperature measurements (b) for the as-solidified 0.02, 0.2, 2 and 5g samples.

homogenized at 1000°C for 24h, then ordered at 700°C for 12h and furnace cooled. After heat treatment, all characterization steps described above were repeated.

3. Results and discussion

3.1. Effect of rapid solidification on microstructure

Fig. 3 presents optical micrographs of the as-solidified Ni-Mn-Ga after etching. The lower magnification images (Fig. 3a–d) show an overview of the grain structure on solidification throughout the entire cross-section of the samples. Elongated columnar grains dominate the structure in the larger (2 and 5g) samples due to unidirectional heat flow through the copper crucible during solidification. Note the difference in magnification between these images. Microstructure analysis was conducted for all samples in the center, corresponding to the location used for assessing characteristic cooling rate from heat transfer analysis. A

close-up of the solidification structure in the center is shown in Fig. 3e–h for all samples at the same magnification for comparison purposes. There is a notable change from cellular-dendritic solidification in the smaller samples (0.02 and 0.2g) to a columnar-dendritic structure in the larger samples (2 and 5g). In addition, an increase in solidification length scale is observed with increasing sample size, indicating a decrease in the characteristic cooling rate. The cell spacing was approximately 10 and 35 μ m in the 0.02 and 0.2g sample, respectively. For the coarser columnar dendrites in the 2 and 5g samples, a primary dendrite arm spacing of approximately 60 and 80 μ m was measured, respectively.

The average bulk composition with standard deviation for the assolidified samples as measured by SEM-EDS analysis is given in Table 1. The measurements did not reveal any distinct compositional change as a function of sample size (i.e., characteristic cooling rate) except for the smallest sample (0.02g) that showed a 2 at.-% decrease in Mn which was mostly replaced by Ni. All samples exhibited standard

Table 2 Structural transformation temperatures obtained from differential scanning calorimetry, Curie temperatures (T_C) obtained from magnetization versus temperature measurements, and saturation magnetization (M_s) at 2 T obtained from magnetization versus applied magnetic field measurements.

Sample	Sample weight	Transformation temperature (°C)							T _C (°C)		$M_s (A/m^2 \bullet kg)$
		T _{s, heating}	T _{s, heating} T _{f, heating}		T _{s, cooling}		T _{f, cooling}				
As-solidified	0.02 g	26	98		95		15		98	a	46.1
	0.2 g	28	97		93		18		97 ^a		61.9
	2 g	27	102		97		15		100 ^a		68.3
	5 g	28	102		97		18		99 ^a		69.0
Sample		Sample weight	Transformation temperature (°C)					T _C (°C)	M _s (A/m ² •kg)		
				A_s	Ap	$A_{\rm f}$	M_s	M _p	M_{f}		
Homogenized (1000°C/1 h + WQ)		0.2 g	53	54	56	43	41	39	97 ^a	67.1	
				57 ^a		61 ^a	54 ^a		51 ^a		
Homogenized and ordered (1000°C/24 h +700°C/12 h +FC)		0.2 g	67 59 ^a	68	70 64 ^a	59 58 ^a	58	57 54 ^a	101 ^a	75.6	

 $^{^{\}rm a}$ Transition temperatures obtained from magnetization curve.

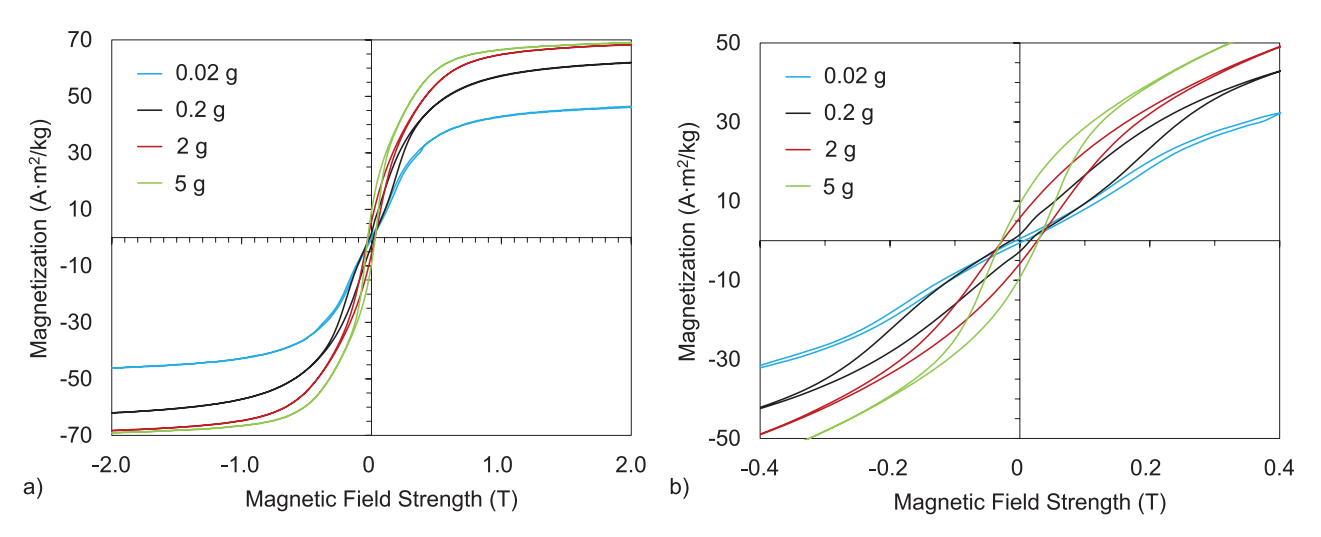


Fig. 7. Representative magnetization hysteresis loops (a) and magnified view of the origin of the hysteresis loops (b) for the as-solidified 0.02, 0.2, 2 and 5g samples. Note the slope changes observed for the 0.2 and 0.02g samples, which are absent from the 2 and 5g sample curves.

deviations of the measured compositions well within the measurement's uncertainty. These standard deviations were measured as the variation between the different point spectra collected at different locations for each sample. Additionally, the count error (measurement uncertainty) for a point spectrum within each sample is reported in Table S1. However, EDS mapping and line scans revealed compositional heterogeneity within the solidification structure (Fig. 4). Elemental partitioning during solidification with enrichment of Mn and corresponding depletion of Ga at the cell and dendrite boundaries was observed for all samples. Additional EDS line scan data is provided as supplemental material (Fig. S1). For quantification purposes, effective partition coefficients (k_{eff}) were determined from the line scan data by dividing the composition measured in the cell/dendrite core (C_C) by the bulk composition (C_0) in the sample center where the line scans were made, i.e., $k_{eff} = C_C$ $/C_{O}$. The calculated k_{eff} values are reported in Table 1. In general, partitioning of Mn and corresponding Ga depletion at the cell and dendrite boundaries increased in severity at larger sample sizes (2 and 5g) as indicated by greater deviation of *k* values from unity.

Microstructures from rapid solidification experiments in the present work were compared to what was observed in the last deposited layer of an actual Ni-Mn-Ga build processed using L-DED [15]. Only the microstructure in the top layer would resemble as-solidified conditions, as simulated in the present work. The multi-layer build-up in L-DED results in local remelting and repeated reheating of preceding layers, which creates regions with various degrees of homogenization throughout the build. The composition of the L-DED deposit was reported as $Ni_{50.9}Mn_{27.5}Ga_{21.6}$, which is close to the Ni-Mn-Ga alloy used here. The top layer of the L-DED sample exhibited a primarily cellular-dendritic solidification structure [15]. The visibility of a solidification structure after etching indicated elemental segregation, but this was not further characterized. The cell spacing was approximately 25 to 30µm. Based on these observations, the rapidly solidified Ni-Mn-Ga in the present work with a sample size of 0.2g and an estimated characteristic cooling rate of 1.1 • 10³K/s most closely resembles the solidification microstructure from L-DED processing.

Further characterization of the as-solidified samples was carried out through XRD to identify the type of martensite present upon rapid cooling. Fig. 5 shows the patterns obtained for each sample, with the dashed line indicators of the 14M peak locations, as well as the non-modulated (NM) martensite and austenite (A) for the additional peaks. The smaller, unidentified peaks are likely martensite modulation peaks, similar to [22]. Although the composition used for this study is primarily reported as 10M martensite [38], internal stresses from rapid solidification and significant compositional inhomogeneities from partitioning

during solidification (observed through EDS) may lead to changes in modulation during cooling. Similar effects have been observed for L-PBF samples of similar composition [16] and on rapidly cooled and pulsed sintered ribbons which showed predominance of NM martensite for the slower cooling and of 14M in the faster cooled alloy [39]. Toman et al. [15] also reported primarily 14M martensite peaks for the as-deposited Ni-Mn-Ga L-DED build with some additional peaks present that could not be identified.

3.2. Effect of rapid solidification on structural and magnetic transition temperatures

Fig. 6a shows heat flow versus temperature curves from DSC for the as-solidified samples. Ni₅₀Mn₂₉Ga₂₁ undergoes a martensitic transition upon cooling from a cubic L21-type austenite structure to a complex martensite structure. The martensite transformation (upon cooling) and the reverse transformation (upon heating) were very broad for all sample sizes. The transformation width ranges from 69 to 75°C for the reverse transformation, and 75-82°C for the martensite transformation. Compared to single crystalline Ni-Mn-Ga, the structural transitions are much broader in the rapid solidified Ni₅₀Mn₂₉Ga₂₁, as expected from non-homogenized samples with composition gradients [22,40]. The broad transitions with slight but multiple deviations (most clear for the 2g and 0.2g samples) are likely indicative of the different transformations that each large grain undergoes, similar to the behavior observed for cast and laser powder bed processed Cu-Al-Mn [41]. From the DSC curves in Fig. 6a, transformation start (T_s) and finish (T_f) temperatures were obtained and are summarized in Table 2. A slight decrease (of about 2–5°C) of the transformation finish ($T_{\rm f}$) temperature on heating and the transformation start (T_s) temperature on cooling were observed in the smaller samples (0.02 and 0.2g). No other changes in structural transition temperatures as a function of sample size were apparent. A decrease in transformation temperatures in rapidly quenched Ni-Mn-Ga ribbons was observed by Chernenko et al. [24] and Heczko et al. [42]. The authors attributed this to a higher degree of quenched-in short range chemical disorder, and/or internal stresses developed during rapid quenching. Wang et al. [25] reported no effect on transformation temperatures at faster solidification in melt-spun Ni-Mn-Ga. The small changes observed in this work may also be related to slight compositional differences between the samples (Table 1). According to previous reports [38,43,44], compositional changes of less than 1 at.-% can shift structural transformation peaks in Ni-Mn-Ga by 1 to 5°C.

Magnetization of the as-solidified samples as a function of

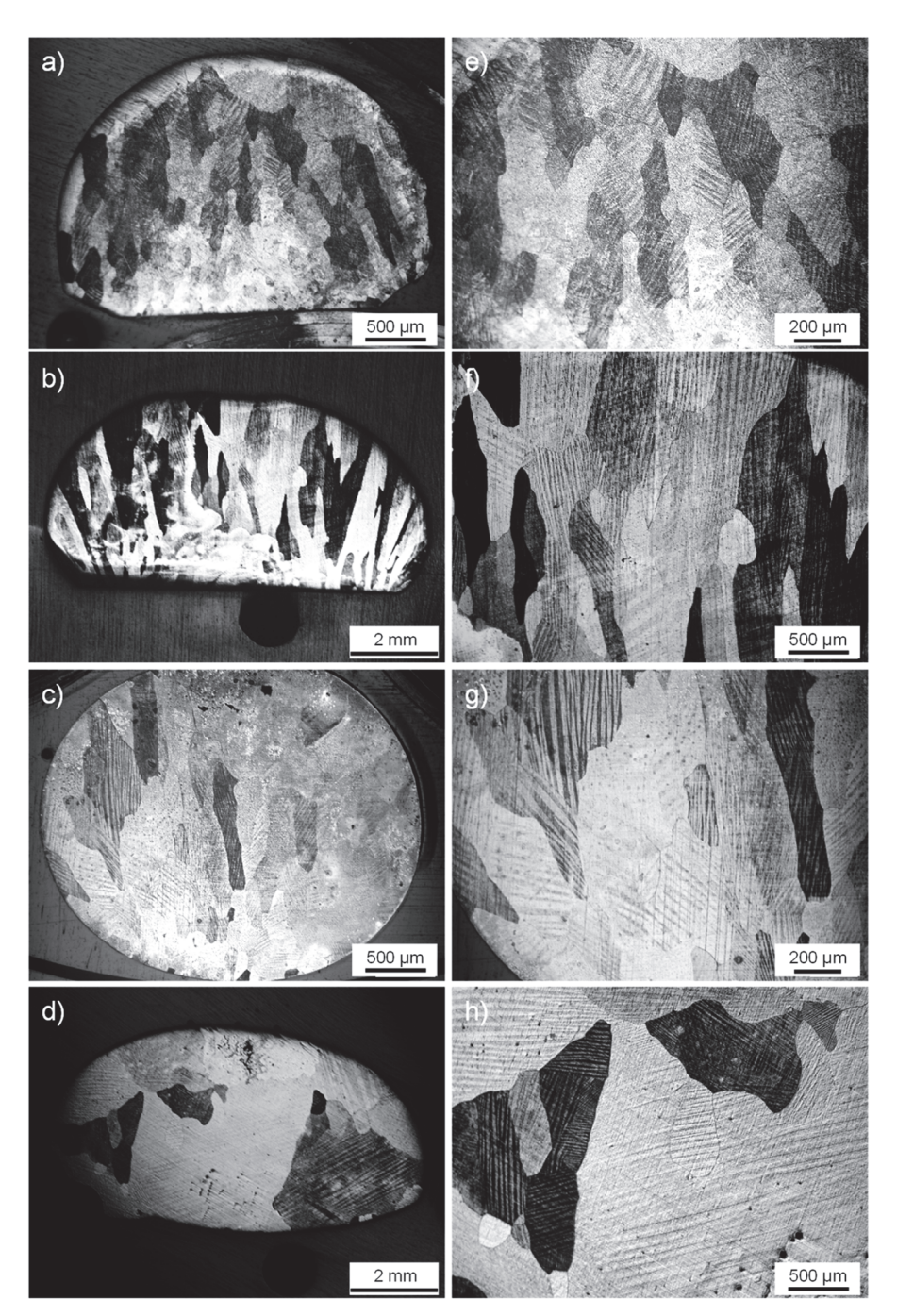


Fig. 8. Optical micrographs (etched) of the microstructure after one-step $(1000^{\circ}\text{C}/1\text{h} + \text{WQ})$ heat-treatment: 0.2g (a, e) and 2g (b, f) sample; and after two-step $(1000^{\circ}\text{C}/24\text{h} + 700^{\circ}\text{C}/12\text{h} + \text{FC})$ heat treatment: 0.2g (c, g) and 2g (d, h) sample. Note the difference in magnification.

temperature is presented in Fig. 6b. The curves mirror the large transformation breadth from DSC. Magnetization increases on heating until a maximum is reached. This increase is almost linear for the smaller samples (0.02 and 0.2g). The Curie temperatures were determined from the curves as indicated in Fig. 6b and summarized in Table 2. The smaller samples (0.02 and 0.2g) showed slightly lower Curie temperatures (by about 2–3°C) as compared to the larger samples (2 and 5g). For melt-spun Ni-Mn-Ga, a decrease in Curie temperature at increasing spinning speed (i.e. faster solidification) has been attributed to quenched-in atomic disorder [24,25,42]. Note that small compositional variations between the samples in this work, as mentioned in the previous section, may also play a role [45].

Structural and magnetic transitions reported for the as-solidified

sample from L-DED processing [15] show good agreement to what is reported for the rapidly solidified Ni-Mn-Ga in this work, even though the L-DED sample likely incorporated multiple, dissimilar microstructural regions with various degrees of homogenization. Toman et al. [15] showed the reverse and martensite transformation breadth to be about 65 and 70° C, respectively. Their DSC curve is very similar in shape to what is presented in Fig. 6a, except that the transformation peaks upon heating and cooling appear shallower and occur at higher temperatures as compared to what was observed in this work. This is likely related to the microstructural heterogeneity of the L-DED sample. The Curie temperature of the as-deposited L-DED sample obtained from VSM measurements was 86° C upon heating, and therefore lower as compared to the rapidly solidified Ni-Mn-Ga in this work. The shape of the

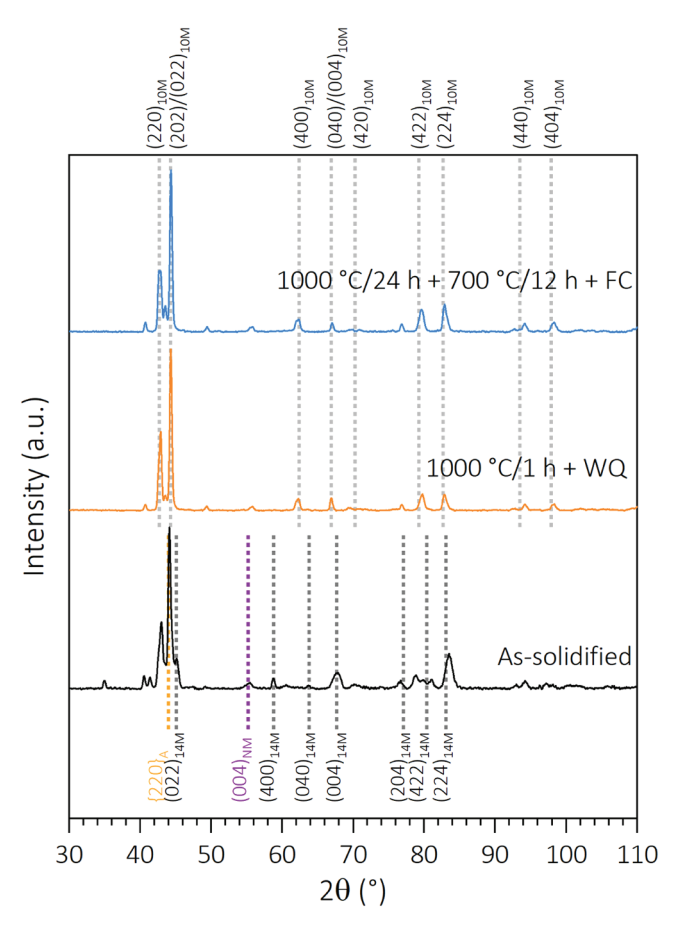


Fig. 9. XRD patterns for the 0.2g as-solidified sample, and after one-step $(1000^{\circ}\text{C}/1h + \text{WQ})$ and two-step $(1000^{\circ}\text{C}/24 \text{ h} + 700^{\circ}\text{C}/12 \text{ h} + \text{FC})$ heat-treatment. Gray dashed lines indicate the positions of 10M martensite peaks as indicated at the top of the plot. The main peaks of the as-solidified sample are highlighted at the bottom for comparison. Small unidentified peaks are attributed to modulation.

magnetization versus temperature curve of the as-deposited L-DED sample exhibited a gradual, almost linear change up to and below the maximum upon heating and cooling, respectively. It most closely resembled what was obtained for the 0.2g sample size in this work (Fig. 6b).

3.3. Effect of rapid solidification on magnetic properties

Fig. 7a presents room temperature magnetization of the as-solidified samples as a function of magnetic field strength (hysteresis loop). The saturation magnetization at 2 T obtained from these plots are listed in Table 2. The saturation magnetization increases with increasing sample size (i.e., decreasing characteristic cooling rate). Note that the saturation could not be fully reached in the available field for any of the sample sizes. The increase in magnetization for less-rapidly solidified samples is attributed to the lesser degree of quenched-in atomic disorder [24,25, 42]. A difference in the shape of the hysteresis loop depending on sample size (i.e., characteristic cooling rate) was observed. To illustrate this more clearly, a magnified view of the origin of the hysteresis loops is presented in Fig. 7b. The hysteresis loops obtained from the larger samples (2 and 5g) exhibit the typical shape of a ferromagnetic material, while those obtained from the smaller samples (0.02 and 0.2g) show changes in the slope of the magnetization upon magnetic field increase and upon reversal. This has been referred to as double-shifted [46] or "wasp-waist" [46-48] hysteresis loop. Also, note that the double-shifted hysteresis loops of the smaller samples (0.02 and 0.2g) are slightly shifted with respect to the magnetization axis.

The observed loop characteristics could be attributed to the proximity effect of anti-phase boundaries (APB) or the presence of internal stresses [49]. Both of which would be expected to increase in the more rapidly solidified samples. Another possible mechanism is exchange anisotropy, usually associated with ferromagnetic-antiferromagnetic coupling [46]. For the rapidly solidified samples in this study, this could be linked to regions with local variations in the Mn content which are a result of Mn partitioning to the cell and dendrite boundaries during solidification (see Section 3.1). Although not associated with changes in the crystal structure, these regions may induce changes in the antiferromagnetic and ferromagnetic coupling of the Mn atoms [46,50]. The smaller samples (0.02 and 0.2g) exhibit a finer solidification structure from more rapid solidification (see Section 3.1), hence the solidification sub-grain boundary area with Mn enrichment is greater as compared to the larger samples (2 and 5g). This may explain why the described loop characteristics are not observed in the latter ones. Toman et al. [15] also reported on a double-shifted hysteresis loop in their as-deposited L-DED sample. This was suggested to be evidence of martensite twin boundary motion [25]. However, the effect would be expected to be larger as demonstrated by Thomas et al. [51] in thin Ni-Mn-Ga films. Also, the fact that in the present study it was only observed in the more rapidly solidified samples indicates that it is rather associated with one or multiple of the above described mechanisms. A detailed investigation on the origin of the observed slope changes was out of the scope of this study.

3.4. Effect of heat treatment

Considerable grain growth was observed after one-step homogenization (1000°C/1 h + WQ) and more so after two-step homogenizationand-ordering heat treatment (1000° C/24 h+ 700° C/12 h + FC) (Fig. 8). For both the one-step and two-step heat treatment, compositional heterogeneity from elemental partitioning during solidification at cell and dendrite boundaries was dissolved. SEM-EDS analysis did not reveal any local variations in Mn or Ga beyond noise and the uncertainty of the measurement itself. XRD results suggest a change from the 14M/NM/A as-solidified martensite to a 10M martensite after the heat treatments, as indicated in Fig. 9, with lattice parameters a=5.99Å, b=5.96Å, and c=5.59Å, based on the pseudotetragonal structure. There does not appear to be a significant change in peak intensity or lattice parameters within the two heat-treatment steps. Results for the 2g samples are provided as supplemental material (Fig. S2). This structural change is consistent with the original composition of the alloy [38], as the microstructure is homogenized, and it is indicative of the transformation temperatures and magnetization changes described below. Recovery of 10M modulation has been observed upon heat treatment for atomized powders [52] and L-PBF foam-like structures [23].

The martensite and reverse transformation breadth was considerably reduced after heat treatment. Fig. 10a compares heat flow versus temperature curves from DSC for the 0.2g sample in as-solidified, homogenized and homogenized-and-ordered conditions. Results for the 2g samples are provided as supplementary material (Fig. S3). In Fig. 10a the progression from very broad transformations in the as-solidified sample (~70-80°C) to very well defined and very narrow transformation peaks after homogenization-and-ordering heat treatment $(\sim 3^{\circ} \text{C})$ is clearly visible. The Curie temperatures are also apparent in the DSC curves of the heat-treated samples as indicated in Fig. 10a. All obtained transformation temperatures are listed in Table 2. Similar transformation temperatures were reported after homogenization for the L-DED processed Ni-Mn-Ga [15] and for L-PBF foams of similar composition [23]. While the transformation breadth is already much improved after the one-step homogenization treatment, additional ordering further narrows the transformation peaks and shifts the transformations to higher temperatures (by about 15°C), as can be seen in Fig. 10a. Toman et al. [15] reported a similar shift to higher

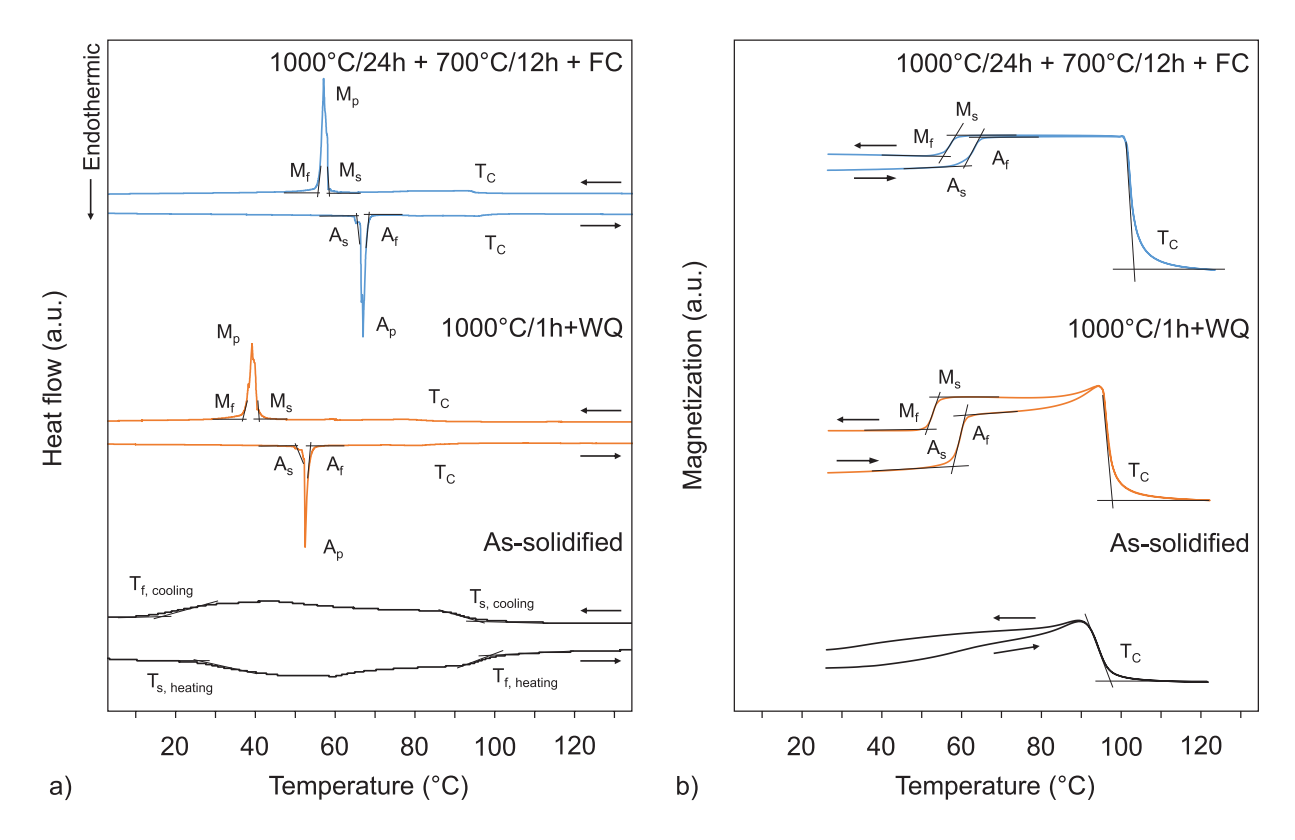


Fig. 10. Heat flow versus temperature curves from DSC (a) and curves from magnetization versus temperature measurements (b) for the 0.2g as-solidified sample, and after one-step (1000° C/1 h + WQ) and two-step (1000° C/24 h+ 700° C/12 h + FC) heat-treatment.

transformation temperatures after homogenization and ordering $(1000^{\circ}\text{C}/24\ h+700^{\circ}\text{C}/12\ h+FC)$ of their L-DED sample (by $\sim 10^{\circ}\text{C})$ and attributed it to slight compositional changes during heat treatment (however smaller than the relative error of EDS analysis) and to the relaxation of residual stresses. Compositional analysis in this work revealed no changes in composition after heat treatment. Residual stresses have been linked to changes in the martensite transformation temperatures in Ni-Mn-Ga thin films [53,54].

Magnetization as a function of temperature for the as-solidified, homogenized and homogenized-and-ordered conditions are shown in Fig. 10b. As already seen from DSC, the transformation breadth is

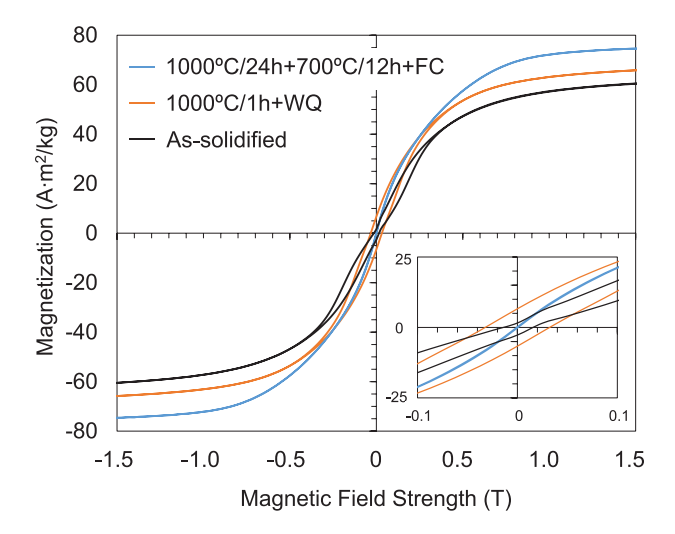


Fig. 11. Magnetization hysteresis loops for the 0.2g as-solidified, homogenized $(1000^{\circ}\text{C}/1h + \text{WQ})$ and homogenized-and-ordered $(1000^{\circ}\text{C}/24h + 700^{\circ}\text{C}/12h + \text{FC})$ samples. Insert is a magnified view of the origin.

reduced after heat treatment. The change in magnetic behavior accompanying the structural transition in Ni50Mn29Ga21 can be clearly observed for the heat-treated samples. On heating, ferromagnetic martensite transforms to ferromagnetic austenite, and then to paramagnetic austenite at the Curie temperature (T_C). During cooling, all transitions occur in reverse order. The Curie temperature is increased from 97°C in as-solidified condition to 101°C after the two-step heat treatment as would be expected based on the more ordered structure [25, 42]. In addition, the greater slope at T_C indicates the improved transformation behavior after homogenization-and-ordering heat treatment. The magnetization hysteresis loops (as a function of field strength) show an increase in the saturation magnetization after heat treatment (Fig. 11). Magnetization is greatest for the homogenized-and-ordered condition. The abnormal slope changes at low field strength and shift along the magnetization axis characteristic for the as-deposited sample (Fig. 7b) were not observed in the heat-treated condition. This further strengthens the argument that these loop characteristics are associated with ferromagnetic-antiferromagnetic exchange interactions from local variations in Mn content or internal stresses (see Section 3.3). Individual plots for the heat treated samples, and the curves for the 2g samples are provided in the supplementary material (Fig. S4 and Fig. S5).

4. Conclusion

In the present work, rapid solidification experiments with varying cooling rates (between $1.1 \cdot 10^2$ and $3.2 \cdot 10^3$ K/s) were conducted on Ni₅₀Mn₂₉Ga₂₁ samples. The resultant microstructure, composition, and magneto-structural properties were compared as a function of cooling rate during solidification, and after two different heat treatments. The findings were then compared to microstructures and properties of an actual Ni-Mn-Ga build processed via laser-based direct energy deposition (L-DED).

The solidification structure changed from columnar-dendritic to

cellular-dendritic at more rapid solidification (i.e., higher cooling rate), while the solidification length scale decreased. All as-solidified samples showed evidence of elemental partitioning during solidification with enrichment of manganese and corresponding depletion of gallium at the cell and dendrite boundaries. Broad martensitic transformations were observed in all samples and proposed to originate from the fine-scale microstructure, chemical heterogeneity and lack of ordering in the assolidified condition. A decrease in magnetization saturation at more rapid solidification was attributed to a higher degree of atomic-disorder. Notably, a double-shifted hysteresis loop that was also slightly shifted with respect to the magnetization axis was observed at more rapid solidification only. This suggests that these hysteresis loop characteristics are associated with ferromagnetic-antiferromagnetic exchange interactions from local variations in Mn content as a result of partitioning during solidification. The finer solidification length scale from more rapid solidification results in more solidification sub-grain boundary area with Mn enrichment, and hence regions that induce changes in the antiferromagnetic and ferromagnetic coupling of the Mn atoms.

Homogenization at 1000°C for 1h was enough to significantly reduce the transformation breadth and increase the magnetization saturation. Homogenization at 1000°C for 24h and ordering heat treatment at 700°C for 12h resulted in considerable grain growth, shifted the transformations to higher temperatures, and further narrowed the transformation peaks. Finally, rapidly solidified samples with an estimated characteristic cooling rate of $1.1 \cdot 10^3\text{K/s}$ most closely resembled the solidification microstructure and magneto-structural properties from L-DED processing. Slight differences in the transformation behavior are likely due to microstructural heterogeneity of the L-DED build.

Overall, the results on rapidly solidified $\rm Ni_{50}Mn_{29}Ga_{21}$ magnetic shape-memory alloy show that microstructural evolution and resultant phase transformation and magnetic properties are strongly dependent on cooling rate during solidification. The addition of a heat treatment can significantly improve magneto-structural properties. These results help to understand cooling rate effects in L-DED additive manufactured Ni-Mn-Ga and to provide post-processing routes that will result in microstructures and properties that enable the magnetic shape-memory effect in Ni-Mn-Ga.

Funding

This work was supported by the National Science Foundation (NSF) through the Division of Materials Research: Topical Materials Research Program (DMR-TMRP) (Grant No. 1808145 and 1808082). We would also like to acknowledge the Manufacturing and Materials Joining Innovation Center (Ma2JIC) made possible through an award from the NSF Industry University Cooperative Research Center (IUCRC) program (Grant No. 1822144), for undergraduate student support through an REU supplement.

Declaration of Competing Interest

The authors declare that they have no known competing financial interests or personal relationships that could have appeared to influence the work reported in this paper.

Acknowledgments

At The Ohio State University, we would like to thank high school intern Ailsa Craigmile and undergraduate students Margaret Lashutka, Allina Molinaro and Frederico Aponte for support with solidification experiments and sample preparation, as well as laboratory technician Wayne Papageorge for support with differential scanning calorimetry. We also gratefully acknowledge graduate student Suraj V. Mullurkara at the University of Pittsburgh, and research scientists Camelia Selcu and Denis Pelekhov at The Ohio State University for assistance with magnetic measurements. Electron microscopy was performed at the Center

for Electron Microscopy and Analysis (CEMAS) at The Ohio State University and at the Nanoscale Fabrication and Characterization Facility (NFCF), a laboratory of the Gertrude E. and John M. Petersen Institute of Nanoscience and Engineering at the University of Pittsburgh. Magnetic measurements were performed at the NanoSystems Laboratory (NSL) at The Ohio State University.

Supplementary materials

Supplementary material associated with this article can be found, in the online version, at doi:10.1016/j.actamat.2023.119325.

References

- D. Musiienko, et al., Giant magnetic-field-induced strain in Ni-Mn-Ga micropillars, Scr. Mater. 150 (2018) 173–176, https://doi.org/10.1016/j. scriptamat.2018.03.020.
- [2] D. Musiienko, et al., Ultrafast actuation of Ni-Mn-Ga micropillars by pulsed magnetic field, Scr. Mater. 162 (2019) 482–485, https://doi.org/10.1016/j. scriptamat.2018.12.009.
- [3] A. Hobza, C.L. Patrick, K. Ullakko, N. Rafla, P. Lindquist, P. Müllner, Sensing strain with Ni-Mn-Ga, Sens. Actuators, A 269 (2018) 137–144, https://doi.org/10.1016/ j.sna.2017.11.002.
- [4] S.J. Murray, M. Marioni, S.M. Allen, R.C. O'Handley, T.A. Lograsso, 6% magnetic-field-induced strain by twin-boundary motion in ferromagnetic Ni–Mn–Ga, Appl. Phys. Lett. 77 (6) (2000) 886–888, https://doi.org/10.1063/1.1306635.
- [5] A. Sozinov, A.A. Likhachev, N. Lanska, K. Ullakko, Giant magnetic-field-induced strain in NiMnGa seven-layered martensitic phase, Appl. Phys. Lett. 80 (10) (2002) 1746–1748, https://doi.org/10.1063/1.1458075.
- [6] A. Sozinov, N. Lanska, A. Soroka, W. Zou, 12% magnetic field-induced strain in Ni-Mn-Ga-based non-modulated martensite, Appl. Phys. Lett. 102 (2) (2013), 021902, https://doi.org/10.1063/1.4775677.
- [7] M. Chmielus, X.X. Zhang, C. Witherspoon, D.C. Dunand, P. Müllner, Giant magnetic-field-induced strains in polycrystalline Ni–Mn–Ga foams, Nature Mater. 8 (11) (2009) 863–866, https://doi.org/10.1038/nmat2527.
- [8] K. Ullakko, Y. Ezer, A. Sozinov, G. Kimmel, P. Yakovenko, V.K. Lindroos, Magnetic-field-induced strains in polycrystalline Ni-Mn-Ga at room temperature, Scr. Mater. 44 (3) (2001) 475–480, https://doi.org/10.1016/S1359-6462(00)00610-2.
- [9] S.L. Taylor, R.N. Shah, D.C. Dunand, Microstructure and porosity evolution during sintering of Ni-Mn-Ga wires printed from inks containing elemental powders, Intermetallics 104 (2019) 113–123, https://doi.org/10.1016/j. intermet.2018.10.024.
- [10] S.L. Taylor, R.N. Shah, D.C. Dunand, Ni-Mn-Ga micro-trusses via sintering of 3D-printed inks containing elemental powders, Acta Mater. 143 (2018) 20–29, https://doi.org/10.1016/j.actamat.2017.10.002.
- [11] M. Caputo, C.V. Solomon, P.K. Nguyen, A.E. Berkowitz, Electron microscopy investigation of binder saturation and microstructural defects in functional parts made by additive manufacturing, Microsc. Microanal. 22 (S3) (2016) 1770–1771, https://doi.org/10.1017/S1431927616009697.
- [12] A. Mostafaei, et al., Microstructural evolution and magnetic properties of binder jet additive manufactured Ni-Mn-Ga magnetic shape memory alloy foam, Acta Mater. 131 (2017) 482–490, https://doi.org/10.1016/j.actamat.2017.04.010.
- [13] A. Mostafaei, P. Rodriguez De Vecchis, E.L. Stevens, M. Chmielus, Sintering regimes and resulting microstructure and properties of binder jet 3D printed Ni-Mn-Ga magnetic shape memory alloys, Acta Mater. 154 (2018) 355–364, https:// doi.org/10.1016/j.actamat.2018.05.047.
- [14] M.P. Caputo, A.E. Berkowitz, A. Armstrong, P. Müllner, C.V. Solomon, 4D printing of net shape parts made from Ni-Mn-Ga magnetic shape-memory alloys, Addit. Manuf. 21 (2018) 579–588, https://doi.org/10.1016/j.addma.2018.03.028.
- [15] J. Toman, P. Müllner, M. Chmielus, Properties of as-deposited and heat-treated Ni-Mn-Ga magnetic shape memory alloy processed by directed energy deposition, J. Alloys Compd. 752 (2018) 455–463, https://doi.org/10.1016/j. iallcom.2018.04.059.
- [16] V. Laitinen, A. Sozinov, A. Saren, A. Salminen, K. Ullakko, Laser powder bed fusion of Ni-Mn-Ga magnetic shape memory alloy, Addit. Manuf. 30 (2019), 100891, https://doi.org/10.1016/j.addma.2019.100891.
- [17] F. Nilsén, I.F. Ituarte, M. Salmi, J. Partanen, S.P. Hannula, Effect of process parameters on non-modulated Ni-Mn-Ga alloy manufactured using powder bed fusion, Addit. Manuf. 28 (2019) 464–474, https://doi.org/10.1016/j. addma.2019.05.029.
- [18] A. Milleret, V. Laitinen, K. Ullakko, N. Fenineche, M.M. Attallah, Laser powder bed fusion of (14M) Ni-Mn-Ga magnetic shape memory alloy lattices, Addit. Manuf. 60 (2022), 103231, https://doi.org/10.1016/j.addma.2022.103231.
- [19] E. Stevens, et al., Microstructural evaluation of magnetocaloric Ni-Co-Mn-Sn produced by directed energy deposition, Microsc. Microanal. 22 (S3) (2016) 1774–1775, https://doi.org/10.1017/S1431927616009715.
- [20] U. Gaitzsch, H. Klauß, S. Roth, L. Schultz, Magnetomechanical training of single crystalline Ni–Mn–Ga alloy, J. Magn. Magn. Mater. 324 (4) (2012) 430–433, https://doi.org/10.1016/j.jmmm.2011.08.008.
- [21] M. Pötschke, et al., Magnetically resetTable 0.16% free strain in polycrystalline Ni–Mn–Ga plates, Scr. Mater. 63 (4) (2010) 383–386, https://doi.org/10.1016/j. scriptamat.2010.04.027.

- [22] V. Laitinen, A. Sozinov, A. Saren, M. Chmielus, K. Ullakko, Characterization of asbuilt and heat-treated Ni-Mn-Ga magnetic shape memory alloy manufactured via laser powder bed fusion, Addit. Manuf. 39 (2021), 101854, https://doi.org/ 10.1016/j.addma.2021.101854.
- [23] I.F. Ituarte, F. Nilsén, V.K. Nadimpalli, M. Salmi, J. Lehtonen, S.P. Hannula, Towards the additive manufacturing of Ni-Mn-Ga complex devices with magnetic field induced strain, Addit. Manuf. 49 (2022), 102485, https://doi.org/10.1016/j. addma.2021.102485.
- [24] V.A. Chernenko, E. Cesari, J. Pons, C. Seguí, Phase transformations in rapidly quenched Ni–Mn–Ga Alloys, J. Mater. Res. 15 (7) (2000) 1496–1504, https://doi. org/10.1557/JMR.2000.0215.
- [25] J. Wang, C. Jiang, R. Techapiesancharoenkij, D. Bono, S.M. Allen, R.C. O'Handley, Microstructure and magnetic properties of melt spinning Ni–Mn–Ga, Intermetallics 32 (2013) 151–155, https://doi.org/10.1016/j.intermet.2012.08.021.
- [26] C.L. Xu, H.Y. Wang, F. Qiu, Y.F. Yang, Q.C. Jiang, Cooling rate and microstructure of rapidly solidified Al–20wt. Si alloy, Mater. Sci. Eng. A 417 (1–2) (2006) 275–280, https://doi.org/10.1016/j.msea.2005.10.040.
- [27] B. Cantor, W.T. Kim, B.P. Bewlay, A.G. Gillen, Microstructure cooling rate correlations in melt-spun alloys, J. Mater. Sci. 26 (5) (1991), https://doi.org/ 10.1007/BF00544465 no. 5, Art. no.
- [28] C. Zhao, et al., Cu-Ni-Sn alloy fabricated by melt spinning and selective laser melting: a comparative study on the microstructure and formation kinetics, J. Mater. Res. Technol. 9 (6) (2020) 13097–13105, https://doi.org/10.1016/j. imt 2020.09.047
- [29] W. Hofmeister, M. Griffith, Solidification in direct metal deposition by LENS processing, JOM 53 (9) (2001) 30–34, https://doi.org/10.1007/s11837-001-0066-
- [30] S.M. Thompson, L. Bian, N. Shamsaei, A. Yadollahi, An overview of direct laser deposition for additive manufacturing; part i: transport phenomena, modeling and diagnostics, Addit. Manuf. 8 (2015) 36–62, https://doi.org/10.1016/j. addma.2015.07.001.
- [31] C. Kenel, C. Leinenbach, Influence of cooling rate on microstructure formation during rapid solidification of binary TiAl alloys, J. Alloys Compd. 637 (Jul. 2015) 242–247, https://doi.org/10.1016/j.jallcom.2015.03.016.
- [32] J. Brillo, et al., Thermophysical properties and thermal simulation of Bridgman crystal growth process of Ni–Mn–Ga magnetic shape memory alloys, Int. J. Heat Mass Transf. 54 (19–20) (2011) 4167–4174, https://doi.org/10.1016/j.iiheatmasstransfer.2011.05.030.
- [33] Y.A. Çengel, A.J. Ghajar, Heat and Mass transfer: Fundamentals & Applications, 4th ed., McGraw-Hill, New York, 2011.
- [34] M.C. Flemings, Solidification processing. in McGraw-Hill series in Materials Science and Engineering, McGraw-Hill, New York, 1974.
- [35] J. Tinoco, H. Fredriksson, Solidification of a modified inconel 625 alloy under different cooling rates, High Temp. Mater. Process. 23 (1) (2004), https://doi.org/ 10.1515/HTMP.2004.23.1.13. Londonno. 1, Art. noJan.
- [36] J.J. Blecher, T.A. Palmer, T. DebRoy, Solidification map of a nickel-base alloy, Metall. Mater. Trans. A 45 (4) (2014) 2142–2151, https://doi.org/10.1007/ s11661-013-2149-1.
- [37] C.A. Schneider, W.S. Rasband, K.W. Eliceiri, NIH image to image J: 25 years of image analysis, Nat. Methods 9 (7) (2012) 671–675, https://doi.org/10.1038/ nmeth.2089.
- [38] N. Lanska, O. Söderberg, A. Sozinov, Y. Ge, K. Ullakko, V.K. Lindroos, Composition and temperature dependence of the crystal structure of Ni–Mn–Ga alloys, J. Appl. Phys. 95 (12) (2004) 8074–8078, https://doi.org/10.1063/1.1748860.

- [39] O. Söderberg, et al., Microstructure and properties of Ni–Mn–Ga alloys produced by rapid solidification and pulsed electric current sintering, J. Alloys Compd. 509 (20) (2011) 5981–5987, https://doi.org/10.1016/j.jallcom.2011.02.166.
- [40] P. Czaja, J. Przewoźnik, M. Kowalczyk, A. Wierzbicka-Miernik, J. Morgiel, W. Maziarz, Microstructural origins of martensite stabilization in Ni49Co1Mn37.5Sn6.5In6 metamagnetic shape memory alloy, J. Mater. Sci. 54 (5) (2019) 4340–4353, https://doi.org/10.1007/s10853-018-3112-8.
- [41] N. Babacan, S. Pauly, T. Gustmann, Laser powder bed fusion of a superelastic Cu-Al-Mn Shape memory alloy, Mater. Des. 203 (2021), 109625, https://doi.org/ 10.1016/j.matdes.2021.109625.
- [42] O. Heczko, P. Svec, D. Janickovic, K. Ullakko, Magnetic properties of Ni-Mn-Ga ribbon prepared by rapid solidification, IEEE Trans. Magn. 38 (5) (2002) 2841–2843, https://doi.org/10.1109/TMAG.2002.802471.
- [43] Y. Ma, C. Jiang, Y. Li, H. Xu, C. Wang, X. Liu, Study of Ni50+xMn25Ga25-x (x=2-11) as high-temperature shape-memory alloys, Acta Mater. 55 (5) (2007) 1533-1541, https://doi.org/10.1016/j.actamat.2006.10.014.
- [44] C. Jiang, G. Feng, S. Gong, H. Xu, Effect of Ni excess on phase transformation temperatures of NiMnGa alloys, Mater. Sci. Eng. A 342 (1–2) (2003) 231–235, https://doi.org/10.1016/S0921-5093(02)00288-5.
- [45] X. Jin, M. Marioni, D. Bono, S.M. Allen, R.C. O'Handley, T.Y. Hsu, Empirical mapping of Ni–Mn–Ga properties with composition and valence electron concentration, J. Appl. Phys. 91 (10) (2002) 8222, https://doi.org/10.1063/ 1.1453943
- [46] A. Deltell, et al., Martensitic transformation, magnetic and magnetocaloric properties of Ni–Mn–Fe–Sn Heusler ribbons, J. Mater. Res. Technol. 12 (2021) 1091–1103, https://doi.org/10.1016/j.jmrt.2021.03.049.
- [47] J.R. Andrez, E.C. Passamani, A.Y. Takeuchi, C. Larica, A. Biondo, Wasp waisted-like hysteresis loops observed in the γ-Fe2MnGa compound, J. Alloys Compd. 701 (2017) 366–371, https://doi.org/10.1016/j.jallcom.2017.01.053.
- [48] L. Tauxe, T.A.T. Mullender, T. Pick, Potbellies, wasp-waists, and superparamagnetism in magnetic hysteresis, J. Geophys. Res. 101 (B1) (1996) 571-583, https://doi.org/10.1029/95JB03041.
- [49] L. Straka, L. Fekete, M. Rameš, E. Belas, O. Heczko, Magnetic coercivity control by heat treatment in Heusler Ni–Mn–Ga(–B) single crystals, Acta Mater. 169 (2019) 109–121, https://doi.org/10.1016/j.actamat.2019.02.045.
- [50] B. Hernando, et al., Magnetocaloric effect in preferentially textured Mn50Ni40In10 melt spun ribbons, Appl. Phys. Lett. 94 (22) (2009), 222502, https://doi.org/ 10.1063/1.3147875
- [51] M. Thomas, et al., Magnetically induced reorientation of martensite variants in constrained epitaxial Ni–Mn–Ga films grown on MgO(001), New J. Phys. 10 (2) (2008), 023040, https://doi.org/10.1088/1367-2630/10/2/023040.
- [52] F. Nilsén, I. Aaltio, Y. Ge, T. Lindroos, S.P. Hannula, Characterization of gas atomized Ni-Mn-Ga powders, Mater Today: Proc. 2 (2015) S879–S882, https://doi. org/10.1016/i.matpr.2015.07.422.
- [53] V.A. Chernenko, M. Kohl, V.A. L'vov, V.M. Kniazkyi, M. Ohtsuka, O. Kraft, Martensitic transformation and microstructure of sputter-deposited Ni-Mn-Ga films, Mater. Trans. 47 (3) (2006) 619–624, https://doi.org/10.2320/
- [54] S. Doyle, et al., Residual stress in Ni-Mn-Ga thin films deposited on different substrates, Eur. Phys. J. Spec. Top. 158 (1) (2008) 99–105, https://doi.org/ 10.1140/epjst/e2008-00660-8.